Journal of Volcanology and Geothermal Research 301 (2015) 180–190

Contents lists available at ScienceDirect

Journal of Volcanology and Geothermal Research

journal homepage: www.elsevier.com/locate/jvolgeores

Fracture of magma containing overpressurised pores

Michael J. Heap [a,*], Tao Xu [b], Alexandra R.L. Kushnir [c], Ben M. Kennedy [d], Chong-feng Chen [b]

[a] Géophysique Expérimentale, Institut de Physique de Globe de Strasbourg (UMR 7516 CNRS, Université de Strasbourg/EOST), 5 rue René Descartes, 67084 Strasbourg cedex, France
[b] Center for Rock Instability & Seismicity Research, Northeastern University, Shenyang 110819, China
[c] Institut des Sciences de la Terre d'Orléans (ISTO), Université d'Orléans, CNRS/INSU, 1A rue de la Férollerie, 45071 Orléans cedex 2, France
[d] Geological Sciences, University of Canterbury, Private Bag 4800, 8140 Christchurch, New Zealand

ARTICLE INFO

Article history:
Received 19 January 2015
Accepted 20 May 2015
Available online 29 May 2015

Keywords:
Overpressure
Magma
Fracture
Fragmentation
Eruption
Brittle

ABSTRACT

Fragmentation is inherent in explosive eruptions. Fragmentation is usually credited to either a critical overpressure during rapid decompression (the fragmentation threshold) or a critical strain achieved during magma ascent. Here, we explore—using an elastic damage mechanics model—a scenario in which magma containing overpressurised pores (as a result of a decompression event, crystallisation-induced pore overpressure, amongst others) experiences a differential stress that can be accommodated elastically. This scenario has previously been overlooked, primarily due to the limitations of the available experimental apparatus: Fragmentation experiments cannot apply a differential stress and deformation experiments require that the applied pore fluid pressure does not exceed the confining pressure. Unaffected by these limitations, our numerical modelling has highlighted that the brittle strength, and the strain required for failure, can be reduced by almost an order of magnitude when the pores within the magma contain an overpressure of just 0.5 MPa. Macroscopic failure of the numerical samples is manifest as a throughgoing fracture and the generation of few fine particles (when compared with experimental rapid decompression fragmentation). In certain scenarios, small differential stresses may therefore act as a trigger for sustained explosive activity if the resultant fracture can penetrate magmas containing high pore pressures or if the fracture encourages flank/dome collapse, thus decompressing magma so that the pores contain overpressures above the fragmentation threshold. Alternatively, the resultant fracture could assist outgassing and thus reduce the explosivity of subsequent eruptions during a particular period of unrest. External stresses, previously unconsidered but invariably present in a dynamic volcanic system, may therefore play a large role in the development and cessation of explosive activity.

1. Introduction

Magma fragmentation is often assigned to one of two mechanisms: (1) Strain- or ascent-driven fragmentation, or (2) rapid decompression fragmentation. The first mechanism, strain- or ascent-driven fragmentation (e.g., Woods and Koyaguchi, 1994; Martí et al., 1999; Papale, 1999; Gonnermann and Manga, 2003; Melnik et al., 2005), occurs due to an increase in strain rate and the structural relaxation time of the magma close to the conduit walls, a consequence of the variation in pressure and gas volume fraction across the conduit (Papale, 1999). The melt phase of the magma will react as a solid if the strain rate is higher than the inverse of the relaxation timescale (Dingwell and Webb, 1990; Dingwell, 1996), leading to magma fragmentation (e.g., Papale, 1999; Gonnermann and Manga, 2003). Strain-induced fragmentation of ascending magma has been associated with sustained explosive eruptions (Papale, 1999) and fracturing/healing cycles during lava extrusion (Tuffen et al., 2003; Kendrick et al., 2014). Indeed, experimental studies have also shown that magmas cross the viscous–brittle transition as strain and strain rate are increased (e.g., Lavallée et al., 2008; Cordonnier et al., 2012; Kendrick et al., 2013; Lavallée et al., 2013; Shields et al., 2014). In the second mechanism, fragmentation is induced when the rapid decompression of pressurised magma results in a decompression wave capable of generating a tensile stress that exceeds the strength of the magma (e.g., Alidibirov and Dingwell, 1996; Zhang, 1999; Koyaguchi et al., 2008). Bubbles of exsolved gases form in magmas as the magma depressurises on its ascent to the surface (Sparks, 1978; Toramaru, 1989; Mangan and Cashman, 1993; Navon and Lyakhovsky, 1998; Gonnermann and Manga, 2012). If the ascent rate is slow compared to the relaxation timescale of the melt phase, the increasing volume of volatiles is accommodated by the growth of bubbles (e.g., Proussevitch and Sahagian, 2005 and references therein). In this scenario, the pressure inside the bubbles (the pore pressure, Pp) will likely equilibrate with the overburden pressure provided by the overlying magma column. However, a pore overpressure (i.e., when the pore pressure is higher than the overburden pressure) can develop if the decompression rate exceeds the rate at which the bubble walls can grow (which is invariably tied to numerous factors, including the volatile content, ascent rate, and viscosity; e.g., Massol and Jaupart, 1999; Proussevitch and Sahagian, 2005; Nguyen et al., 2014). For example,

* Corresponding author.
E-mail address: heap@unistra.fr (M.J. Heap).

http://dx.doi.org/10.1016/j.jvolgeores.2015.05.016
0377-0273/

pore overpressure can develop due to crystallisation of magma driving local volatile oversaturation and the exsolution of volatiles into isolated pores (e.g., Tait et al., 1989; Sparks, 1996; Stix et al., 1997). Local pore overpressures can be generated if a low permeability magma plug (Michaut et al., 2009; Yokoo et al., 2009) or low permeability country rock (Jaupart, 1998; Kennedy et al., 2010) impedes gas movement and ultimate escape. Larger overpressures can exist following rapid decompression triggered by dome/sector collapse or fracture propagation (i.e., the magma is suddenly exposed to atmospheric pressure; e.g., Alidibirov and Dingwell, 1996). For a given porosity, if the pore overpressure exceeds a critical pressure—coined the fragmentation threshold (e.g., Alidibirov and Dingwell, 1996)—the resultant decompression wave results in an expansion of gas sufficient to break the bubble walls and fragment the magma. Magma overpressure driven fragmentation has been associated with a wide variety of volcanic activity (Massol and Jaupart, 1999 and references therein), from Vulcanian explosions (e.g., Druitt et al., 2002; Kennedy et al., 2005; Burgisser et al., 2010; Cole et al., 2014) to Plinian eruptions (e.g., Walker and Croasdale, 1970). As a result, considerable attention has been devoted to understanding and quantifying the fragmentation threshold of magma. Experimental studies, for example, have shown that the fragmentation threshold is inversely and nonlinearly dependent on connected porosity (e.g., Alidibirov and Dingwell, 1996; Martel et al., 2000, 2001; Spieler et al., 2004; Kueppers et al., 2006; Scheu et al., 2008).

In this study we envisage a scenario where external differential stresses are acting on the magma within a conduit. Such external stresses are likely ubiquitous in a highly stressed volcanic system on the verge of an explosive eruption (e.g., Gerst and Savage, 2004; Roman et al., 2004). If the strain rate is sufficiently high, or the magma is sufficiently viscous, these stresses may be accommodated elastically by the magma. In our scenario, the magma contains a pore overpressure that is insufficient to fragment the magma (i.e., the resultant pore overpressure is lower than the fragmentation threshold). This pore overpressure could exist due to a number of reasons, for example: Crystallisation, decompression fracture, and sector/dome collapse, amongst others. The motivation of this study is to assess whether elastically accommodated external differential stresses can fragment magma containing a pore overpressure (below the fragmentation threshold) and, if so, to evaluate the magnitudes of stresses and strains required and the style and characteristics of brittle failure. Until now, the influence of external differential stresses and strains on the fragmentation or failure of magmas containing a pore overpressure has not been explored specifically: Experimental studies of overpressure-driven fragmentation have been performed in the absence of an imposed differential stress (e.g., Spieler et al., 2004) and triaxial deformation experiments (e.g., Cordonnier et al., 2012) require that the confining pressure is greater than the applied pore pressure. To explore this concept, we employ an elastic damage mechanics model—the two-dimensional flow-coupled Rock Failure and Process Analysis code model (e.g., Tang et al., 2002)—to deform numerical samples containing overpressurised pores. A similar model has recently shown that, in the absence of a pore overpressure, porosity and pore size play crucial roles in dictating the brittle strength of volcanic rocks and magmas (Heap et al., 2014). We briefly describe the model before presenting the influence of porosity and pore size on the failure of magmas containing pore overpressures (at overpressures below the classically defined fragmentation threshold). Finally, we demonstrate the implications of the model output using simple conceptual volcanic scenarios.

2. Description of the model and simulations

Owing to their flexibility, elastic damage mechanics models have been used to investigate damage accumulation and failure in a number of scientific disciplines, including, and not limited to: Geophysics (e.g., Tang et al., 2003), geology (e.g., Lacroix and Amitrano, 2013), engineering (e.g., Xu et al., 2006), and volcanology (e.g., Heap et al., 2014). Recently, Heap et al. (2014) demonstrated that output from the Rock Failure and Process Analysis code model (Tang, 1997) is qualitatively similar to model predictions from the micromechanical model of Sammis and Ashby (1986).

The two-dimensional flow-coupled Rock Failure and Process Analysis code (F-RFPA^{2D}) model (e.g., Tang et al., 2002, 2004; Wang et al., 2013), used in this study, assumes that the melt within the magma reacts in an elastic (i.e., the stress is not dissipated viscously) and brittle manner (i.e., the melt acts as a solid and, as a result, the pores are stationary) to an external stress. As a result, the start of our model (time and strain equal zero) corresponds to the time when magmas containing a pore overpressure first experience a differential stress that can be accommodated elastically. Although a time-dependent RFPA model exists (Xu et al., 2012), we have chosen to use a time-independent model because, under the high strain rates implicated by a brittle response, there is insufficient time for time-dependent subcritical processes (such as stress corrosion cracking, see Heap et al., 2011) to influence the mechanical behaviour of the deforming magma. In this study we adopt the convention that compressive stresses and strains are positive.

The two-dimensional numerical samples of this study—40 mm in length and 20 mm in width—consist of 80,000 square elements with sides of 0.1 mm. The elements within the sample were assigned the same mean physical and mechanical properties (Table 1) used in Heap et al. (2014). To reflect material heterogeneity on the microscale (variations in glass strength, microlite number density, amongst others), each 0.1 mm square element is assigned a value of residual uniaxial strength (compressive σ_{cr} and tensile σ_{tr}) and Young's modulus E_0 using a Weibull probability density function (Weibull, 1951; Wong et al., 2006):

$$x(u) = \frac{m}{u_o}\left(\frac{u}{u_o}\right)^{m-1} \exp\left[-\left(\frac{u}{u_o}\right)^{m}\right] \quad (1)$$

where $x(u)$ is either $\sigma_{cr}(u)$, $\sigma_{tr}(u)$ or $E_0(u)$, where u is the scale parameter of an individual element and u_0 is the scale parameter of the average element (both of which depend on the parameter in question). We have chosen to let the Weibull shape parameter be $m = 3$ (the homogeneity index) for in all of our numerical simulations, the same value used in Heap et al. (2014). Low values of m ($m < 3$) result in heterogeneous samples and high values of m ($m > 3$) result in homogeneous samples. An example of the distribution of Young's modulus and uniaxial compressive strength using $m = 3$, for a sample with the mean element physical and mechanical properties given in Table 1 (containing 80,000 elements), is presented as Fig. 1. The modelled uniaxial compressive strength of a numerical sample containing 0% porosity and a homogeneity index $m = 3$ was found to be 553 MPa (Heap et al., 2014). The strength of porosity-free borosilicate glass is about 600 MPa at a temperature of 535 °C and a strain rate of 10^{-3} s^{-1} (Vasseur et al., 2013), serving to validate our approach and choice of mean physical and mechanical properties (Table 1) and Weibull shape parameter m.

We introduced porosity (5 or 25%) into our numerical samples in the form of circular pores (diameter of either 0.5 or 1.0 mm). The pores were placed in the samples at random and without overlap (i.e., all of the porosity is isolated). Examples of the numerical samples are given

Table 1
The physical and mechanical properties of the groundmass used in the Rock Failure and Process Analysis code (RFPA$_{2D}$) stochastic modelling. The same input values were used in Heap et al. (2014).

Homogeneity index	3
Mean uniaxial compressive strength [MPa]	2300
Mean Young's modulus [GPa]	100
Poisson's ratio	0.25
Ratio of compressive to tensile strength	10
Frictional angle [degrees]	30

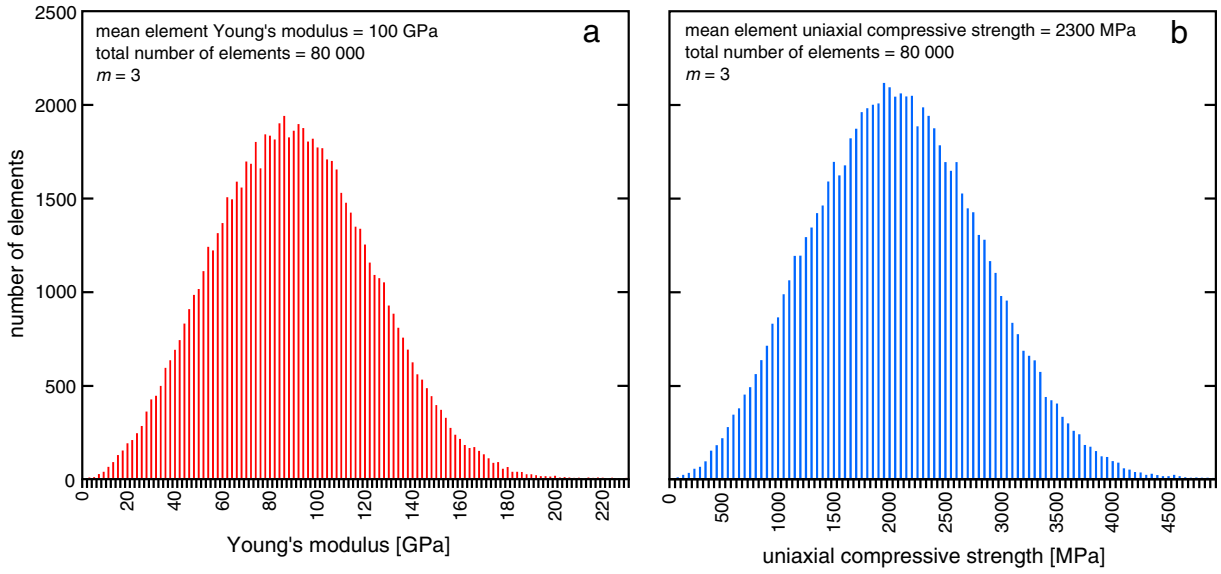

Fig. 1. Example of the distribution of (a) Young's modulus and (b) uniaxial compressive strength for a sample with the mean element physical and mechanical properties given in Table 1 and a Weibull shape factor $m = 3$ (the homogeneity factor). The sample contains 80,000 elements.

as Fig. 2a. For each combination of porosity and pore size, we prepared numerical samples that contained pore pressures (Pp) of 0.5, 1, 2, 3, and 5 MPa (Fig. 2b). We flank the simulations of this study with those performed with a pore pressure of 0 MPa presented in Heap et al. (2014). Since the simulations are unconfined (i.e., the confining pressure $Pc = \sigma_3 = 0$ MPa) the implemented pore pressures can be considered as overpressures by adopting a simple effective pressure law where the effective pressure $Peff = Pc - \alpha Pp$; we assume that poroelastic constant $\alpha = 1$. The overpressures used in the simulations of this study are all below the fragmentation threshold (P_{th}) defined by the following relationship (Koyaguchi et al., 2008):

$$P_{th} = \frac{2S_3(1-\Phi)}{3\Phi\sqrt{\Phi^{-1/3}-1}} \quad (2)$$

where Φ is the porosity and S_3 is an effective tensile strength. Eq. (2) yields fragmentation threshold values of 19.3 and 5.2 MPa for 5% and 25% porosity, respectively (taking $S_3 = 2$ MPa).

The stress–strain behaviour of the solid elements within the model is governed by linear elastic theory and the generalised effective stress principal of Terzaghi such that (e.g., Tang et al., 2002, 2004; Wang et al., 2013):

$$\sigma'_{ij} = \sigma_{ij} - \alpha P f \delta_{ij} = \lambda_L \delta_{ij} \varepsilon_v + 2G\varepsilon_{ij} \quad (3)$$

where σ'_{ij} is the effective stress tensor ($i,j = 1, 2, 3$), σ_{ij} and ε_{ij} are the stress and strain tensors, respectively, δ_{ij} is the Kronecker delta, λ_L is Lame's constant, G is the shear modulus, and ε_v is the volumetric strain where $\varepsilon_v = \varepsilon_{11} + \varepsilon_{22} + \varepsilon_{33}$. Although the F-RFPA$_{2D}$ model has been previously used to determine permeability during deformation using equations adapted from Biot's (1941) theory of consolidation (e.g., Tang et al., 2002; Xu and Tang, 2008), we use the model here to simply deform samples containing pores with a pore fluid pressure (i.e., there is no "seepage" in the simulations presented herein). The stress around a pore containing a pore fluid overpressure is therefore a combination of the stress field induced by a circular hole and the additional stress field provided by the fluid pressure (Eq. (3); Tang et al., 2002). To demonstrate the influence of a pore overpressure on the tensile stress field surrounding a pore, we performed two supplementary simulations in which we applied an external stress (a compressive stress of 1 MPa)

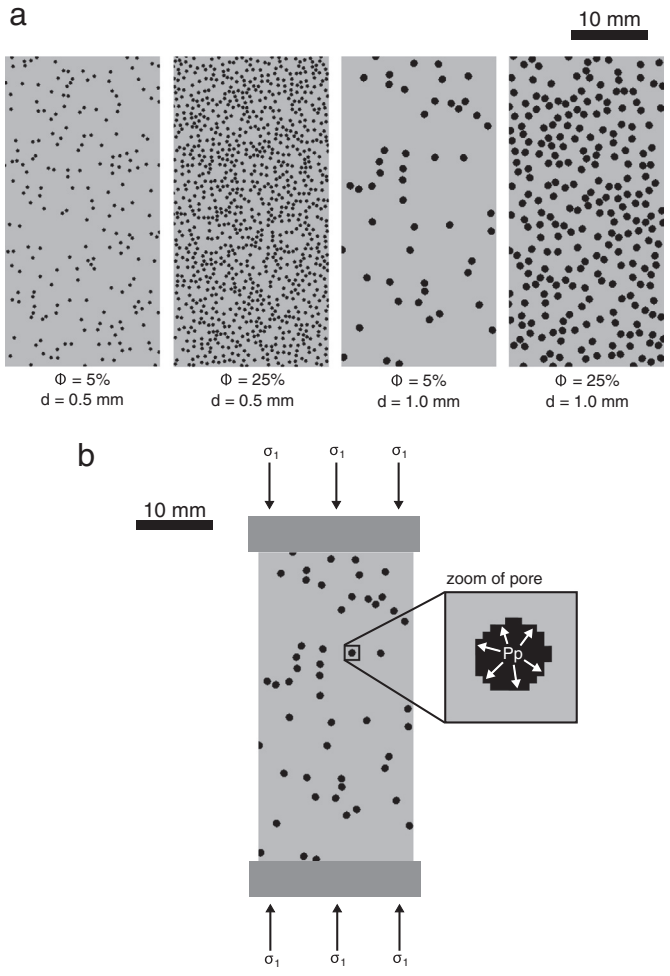

Fig. 2. (a) Examples of the numerical samples (20 mm in width and 40 mm in length) used in this study. The groundmass is grey and the porosity black. The porosity (Φ) and the pore diameter (d) are given under each sample. (b) The pressures acting on a sample in the model. Pp = pore fluid pressure; σ_1 = axial pressure. In our simulations $Pp > Pc = 0$ MPa.

to a 10 × 10 mm square sample containing a central pore with a diameter of 1 mm (Fig. 3). The tensile stress fields for the simulations, in which the central pore contained no pressure and 1 MPa overpressure, are presented as Fig. 3b and c, respectively, and stress profiles (from B, the edge of the sample, to A, the edge of the pore; Fig. 3a) for both simulations are provided as Fig. 3c. The stress profiles show that the tensile stress within the elements near the pore is much higher in the presence of a pore overpressure. In detail, the pore overpressure increases the tensile stress on elements up to 1.5 mm from the pore. We note that the model only considers the mechanical influence of a pore fluid pressure (Eq. (3)); the chemical influence of the presence of a fluid phase, such as the reduction of surface free energy and subcritical cracking mechanisms (e.g., Baud et al., 2000; Brantut et al., 2013), is neglected. However, as discussed above, we consider that the strain rates implicated by a solid response of the melt are too high for subcritical crack growth processes to exert any significant influence on the deformation.

The 40 × 20 mm numerical samples of this study were deformed uniaxially ($\sigma_1 > \sigma_2 = \sigma_3 = 0$; Fig. 2b) in 0.002 mm increments (corresponding to strain increments of 0.005%). Following each uniaxial loading increment, the stress acting upon each 0.1 mm element was calculated:

$$\sigma_1 = E_0(1-D)\varepsilon_1 \tag{4}$$

where σ_1 is the axial stress, D is the isotropic damage variable, and ε_1 is the axial strain. If no elements were damaged in a particular loading increment, the numerical sample was simply subjected to the next 0.002 mm displacement increment. However, an element is damaged if the stress acting on the element meets one of the two strength criteria, the maximum tensile strain criterion:

$$D = \begin{cases} 0 & \varepsilon > \varepsilon_{t0} \\ 1 - \dfrac{\sigma_{tr}}{\varepsilon E_0} & \varepsilon_{tu} \le \varepsilon < \varepsilon_{t0} \\ 1 & \varepsilon < \varepsilon_{tu} \end{cases} \tag{5}$$

or the Mohr–Coulomb criterion:

$$D = \begin{cases} 0 & \varepsilon < \varepsilon_{c0} \\ 1 - \dfrac{\sigma_{cr}}{\varepsilon E_0} & \varepsilon \ge \varepsilon_{c0} \end{cases} \tag{6}$$

where ε_{tu} is the ultimate tensile strain of the element, and $\sigma_{tr} = \lambda\sigma_{t0}$ (where λ is the residual strength coefficient, and σ_{t0} is the uniaxial tensile strength at the elastic strain limit, ε_{t0}); and where the residual uniaxial compressive strength σ_{cr} is defined as $\sigma_{cr} = \lambda\sigma_{c0}$ (where λ is the residual strength coefficient, and σ_{c0} is the uniaxial compressive strength at the elastic strain limit). When an element is damaged its Young's modulus is modified according to the following elastic damage constitutive law (Lemaitre and Chaboche, 1990):

$$E = E_0(1-D) \tag{7}$$

where E_0 is the Young's modulus of the damaged element. We note that, although Eq. (7) stipulates that the Young's modulus of an element is 0 GPa when $D = 1$ (completely damaged), the programme assigns a value of 1.0×10^{-5} GPa to prevent the system of equations from being ill-posed. The tensile strength criterion was more likely to be met since the tensile strength has been set as 1/10 of the compressive strength (Table 1; Jaeger et al., 2007). If any elements were damaged in a particular displacement increment, the distribution of stress and pore pressure within the sample were recalculated; this process continued until only very few elements were damaged, at which point the numerical sample was subjected to the next 0.002 mm displacement increment. As a result, there is no deformation rate sensu stricto: The numerical samples are deformed so that the rate of deformation does not exceed the evolution of the microstructure. However, since the melt of the magma within in the model reacts as an elastic solid, fast

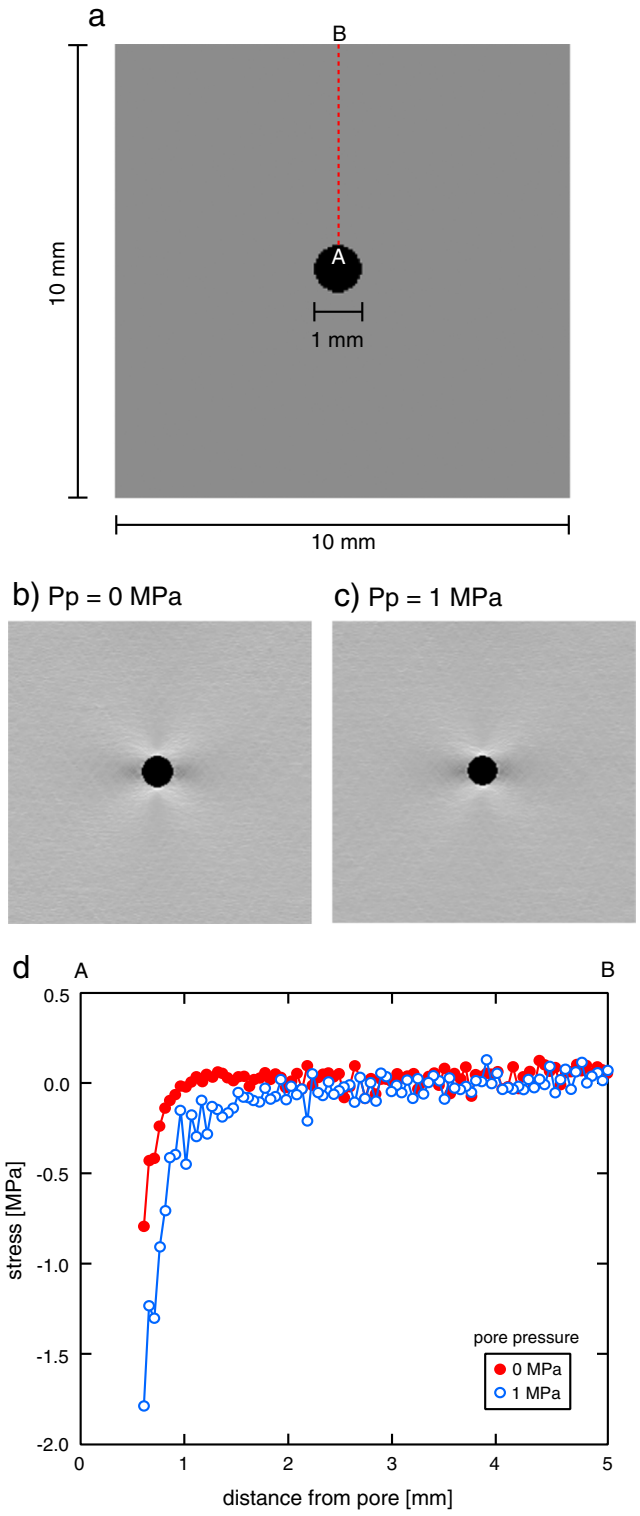

Fig. 3. Simulations designed to illustrate the influence of a pore overpressure on the stress field surrounding a circular pore. (a) The model setup. The square (10 × 10 mm) sample contains a central pore that is 1 mm in diameter. The mean element physical and mechanical properties are given in Table 1 and the Weibull shape factor $m = 3$. (b) Tensile stress field surrounding a pore that contains no internal pore pressure. Lighter colours correspond to higher tensile stresses. (c) Tensile stress field surrounding a pore that contains an internal pore pressure of 1 MPa. Lighter colours correspond to higher tensile stresses. (d) A stress profile from B to A (see panel (a)) for the simulations containing pore overpressures of 0 and 1 MPa shown in panels (b) and (c).

deformation rates are implicit. This procedure continued until macroscopic sample failure. A flow chart showing the procedure is given as Fig. 4.

3. Results

We investigated brittle failure in magma containing different values of porosity (5% and 25%), pore sizes (diameters of 0.5 and 1.0 mm), and pore overpressures below the classically defined fragmentation threshold (i.e., 0.5, 1, 2, 3, and 5 MPa; Table 2). Examples of the simulated stress–strain curves (porosity = 5%; pore diameter = 0.5 mm) for samples containing pore overpressures of 0.5, 1, 2, 3, and 5 MPa are shown in Fig. 5. Firstly, it is important to note that the stress–strain curves produced by the model are similar to those observed for laboratory uniaxial compressive strength experiments (e.g., Hoek and Bieniawski, 1965; Brace et al., 1966; Scholz, 1968; Vasseur et al., 2013). In all of our simulations, the samples failed macroscopically, marked in the stress–strain curves by a sharp stress drop. Macroscopic sample failure, in all our numerical samples, was manifest as a throughgoing fracture and the generation of few fine (ash-sized) particles, examples of which are given in Fig. 6.

Synopsis plots showing the influence of porosity, pore size, and pore overpressure on the stress and strain required for macroscopic failure are provided as Figs. 7 and 8. Globally, Figs. 7 and 8 show that stress and strain required for failure are reduced dramatically as the pore overpressure is increased from 0 to 0.5 MPa. For example, at a porosity of 5% and a pore diameter of 0.5 mm, strength was reduced from ~290 to ~50 MPa as the pore overpressure was increased from 0 to 0.5 MPa (Fig. 7c). However, the stress and strain required for failure does not change significantly as pore overpressure is increased from 0.5 to 5 MPa (Figs. 7 and 8; see also Table 2).

Table 2
Model output summary of the 25 $RFPA_{2D}$ simulations used in this study.

Total porosity [%]	Pore diameter [mm]	Pore overpressure [MPa]	Axial strain required for failure [%]	Axial stress required for failure [MPa]
5[a]	0.5	0	0.4625	291.2
5	0.5	0.5	0.0700	50.2
5	0.5	1	0.0375	27.3
5	0.5	2	0.0725	52.9
5	0.5	3	0.0650	48.2
5	0.5	5	0.0550	42.1
5[a]	1.0	0	0.4125	229.8
5	1.0	0.5	0.0575	41.1
5	1.0	1	0.0650	24.0
5	1.0	2	0.0550	40.1
5	1.0	3	0.0450	18.1
5	1.0	5	0.0100	6.0
25[a]	0.5	0	0.2875	86.2
25	0.5	0.5	0.0475	17.2
25	0.5	1	0.0650	46.4
25	0.5	2	0.0425	16.1
25	0.5	3	0.0350	26.6
25	0.5	5	0.0650	48.8
25[a]	1.0	0	0.3250	75.8
25	1.0	0.5	0.0400	14.5
25	1.0	1	0.0200	7.5
25	1.0	2	0.0200	8.2
25	1.0	3	0.0300	5.2
25	1.0	5	0.0100	6.3
25	1.0	5	0.0100	6.0

[a] Simulation taken from Heap et al. (2014).

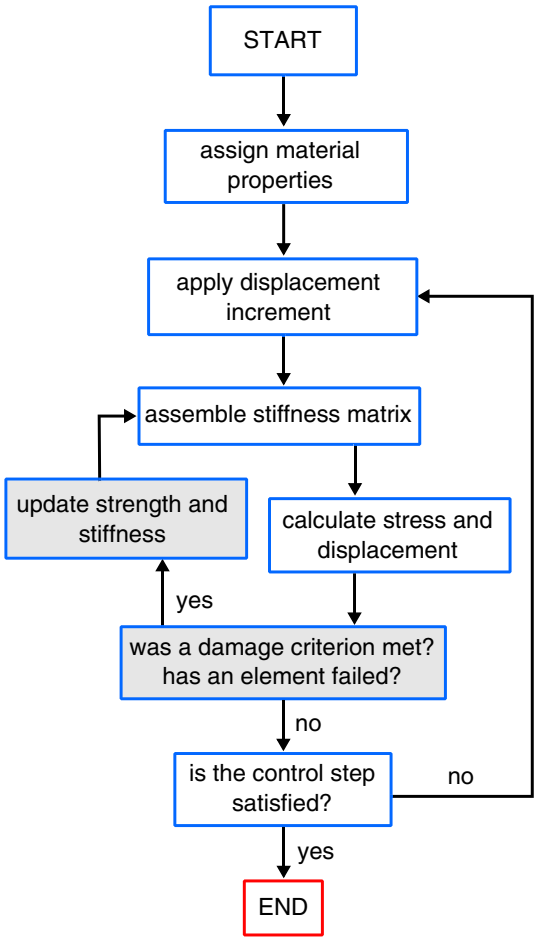

Fig. 4. A flow chart outlining the procedure for the Rock Failure and Process Analysis code. Modified from Heap et al. (2014).

The model output shown in Fig. 7 highlights the influence of porosity on the strain (Fig. 7a and b) and stress (Fig. 7c and d) required for failure. Over the range of pore overpressures tested (0 to 5 MPa), the 25% porosity samples (represented by circles) failed at stresses and strains that are, in most cases, lower than their 5% porosity counterparts (represented by squares; Fig. 7), although we note that the difference in strength between the 5% and 25% porosity samples is essentially negligible at a pore overpressure of 5 MPa.

The model output shown in Fig. 8 highlights the influence of pore size on the strain (Fig. 8a and b) and stress (Fig. 8c and d) required for failure. Over the range of pore overpressures tested (0 to 5 MPa), the samples containing 1.0 mm pores (represented by the open symbols) failed at stresses and strains that are, in most cases, lower than those samples containing 0.5 mm diameter pores (represented by the filled symbols; Fig. 8).

4. Discussion

4.1. Model interpretation

In our model, a circular void locally amplifies the stress (Sammis and Ashby, 1986; Jaeger et al., 2007) and, during deformation, promotes pore-emanating microcracks that grow from the pore wall and eventually coalesce leading to macroscopic failure (see Heap et al., 2014). However, in the presence of a pore overpressure, the tensile stress lobes at the north and south poles (those parallel to the direction of the maximum principal stress) of the pore are magnified further (see Fig. 3). This further stress amplification allows pore-emanating cracks to develop more easily, explaining the reduction in the strain and stress required for failure in the presence of a pore overpressure. Ultimately, when an overpressure is present, the failure mode is identical to that for simulations performed with no overpressure (i.e., the simulations shown in Heap et al., 2014): Pore-emanating cracks, orientated parallel to the maximum principal stress, coalesce to form a throughgoing

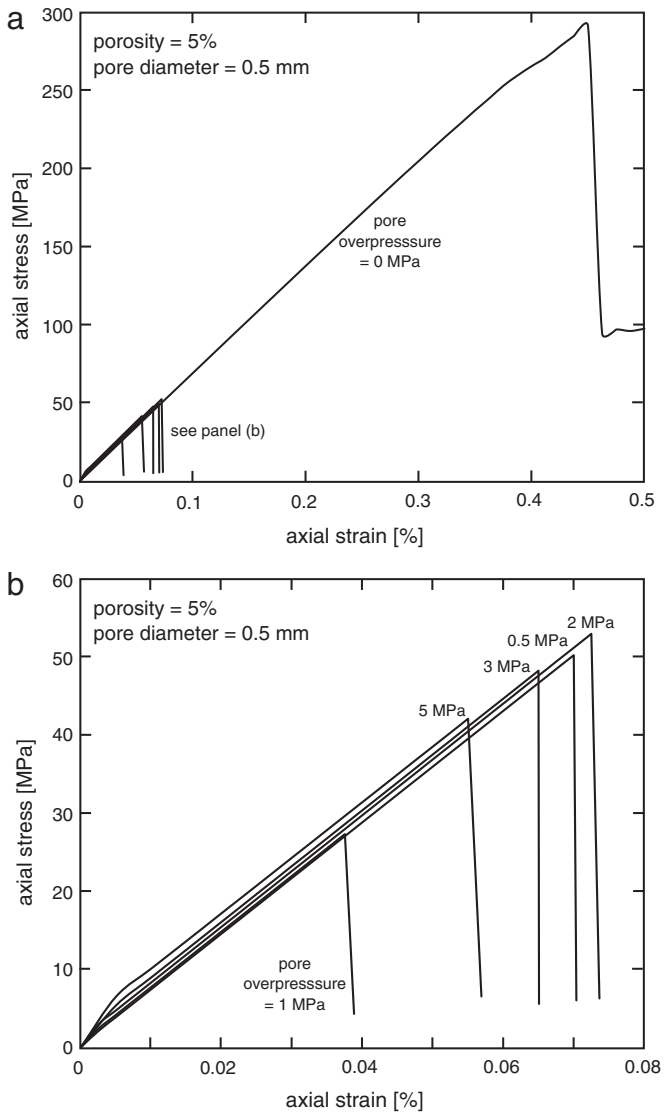

Fig. 5. Examples of the modelled stress–strain curves. (a) Stress–strain curves for numerical samples containing 5% porosity and pores 0.5 mm in diameter. The curves shown are for samples containing pore overpressures of 0, 0.5, 1, 2, 3, and 5 MPa. (b) Stress–strain curves for numerical samples containing 5% porosity and pores 0.5 mm in diameter. The curves shown are for samples containing pore overpressures of 0, 0.5, 1, 2, and 3 MPa.

fracture (as observed in the post-failure snapshots shown in Fig. 6). The macroscopic fracture often nucleates from pore clusters (i.e., locally high porosities), also in accordance with the observations of Heap et al. (2014). We find, perhaps surprisingly, that the stress and strain required for failure does not change drastically as pore overpressure is increased from 0.5 MPa to 5 MPa (Figs. 7 and 8). It is likely therefore that the amplification of tensile stresses at a pore overpressure of 0.5 MPa is sufficient to form pore-emanating cracks and trigger runaway sample failure at low external differential stresses.

The model output shows that the 25% porosity samples fail at lower stresses and strains than those containing a porosity of 5% (Fig. 7). In other words, over the range of pore overpressures investigated herein (0 to 5 MPa), sample porosity still exerts a control on the mechanical behaviour. As for the simulations of Heap et al. (2014), the reduction in the stress and strain required for failure as porosity is increased from 5% to 25% can be explained by the increased likelihood of pore clustering at higher porosities. Pore clustering further amplifies local stresses by promoting the overlap and interaction of the tensile stress lobes of neighbouring pores. It follows that higher local stresses allow pore-emanating cracks to develop at lower external differential stresses.

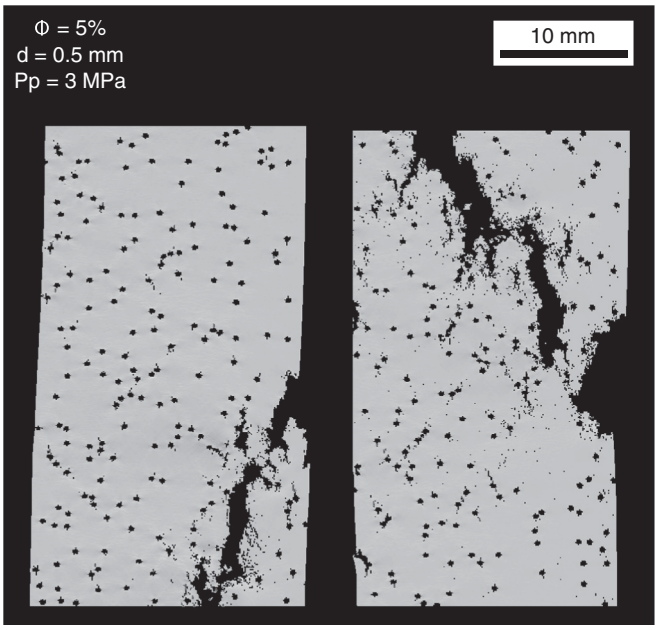

Fig. 6. Examples of macroscopic failure in the numerical samples. The snapshots show macroscopic failure in two samples, both containing a porosity of 5%, a pore diameter of 0.5 mm, and a pore overpressure of 3 MPa.

Our modelling also shows that, at a constant value of porosity, samples containing pore diameters of 1.0 mm, for the most part, fail at lower stresses and strains than those containing pore diameters of 0.5 mm (Fig. 8). As for the influence of porosity, we can conclude that, over the tested range of overpressures, pore size can still influence the mechanical behaviour. Larger pores generate higher stress intensities at the crack tips (Sammis and Ashby, 1986), allowing pore-emanating cracks to propagate at low differential stresses, and permit a shorter route for macroscopic failure (Heap et al., 2014).

We also notice that macroscopic failure in the presence of a pore overpressure appears more localised than the accumulation of damage within numerical samples containing no pore overpressure (as in Heap et al., 2014). Deformation in the absence of a pore overpressure typically involved the growth and development of several large (2–3 mm) pore-emanating cracks; eventually one of these cracks, perhaps favourably orientated or located within a zone containing a higher pore number density, developed into the macroscopic fracture that resulted in sample failure (Heap et al., 2014). By contrast, in the presence of a pore overpressure, and likely due to the increased crack tip stress intensity, once a crack reaches an appreciable length (above about 0.2–0.3 mm) it grows at the expense of the others and develops into a throughgoing macroscopic fracture. Elsewhere in the sample, pore-emanating cracks only reach lengths of about 0.2 mm (Fig. 6). However, and as discussed above, the style of macroscopic failure—a throughgoing fracture—was unaffected by the presence of a pore overpressure (Fig. 6; Heap et al., 2014).

4.2. Volcanological significance

Experimentally, magma has been shown to fail in a brittle manner when deformed in compression at high strain rates (e.g., the uniaxial experiments of Lavallée et al., 2008; Kendrick et al., 2013; Lavallée et al., 2013). Our model shows that, when magma can react to an external stress elastically (i.e., at high strain rates), a pore overpressure of as little as 0.5 MPa can drastically reduce the stress and strain required for failure. We also find that, for a constant value of pore overpressure, magmas containing higher porosities or larger pore diameters will fail at lower stresses and strains.

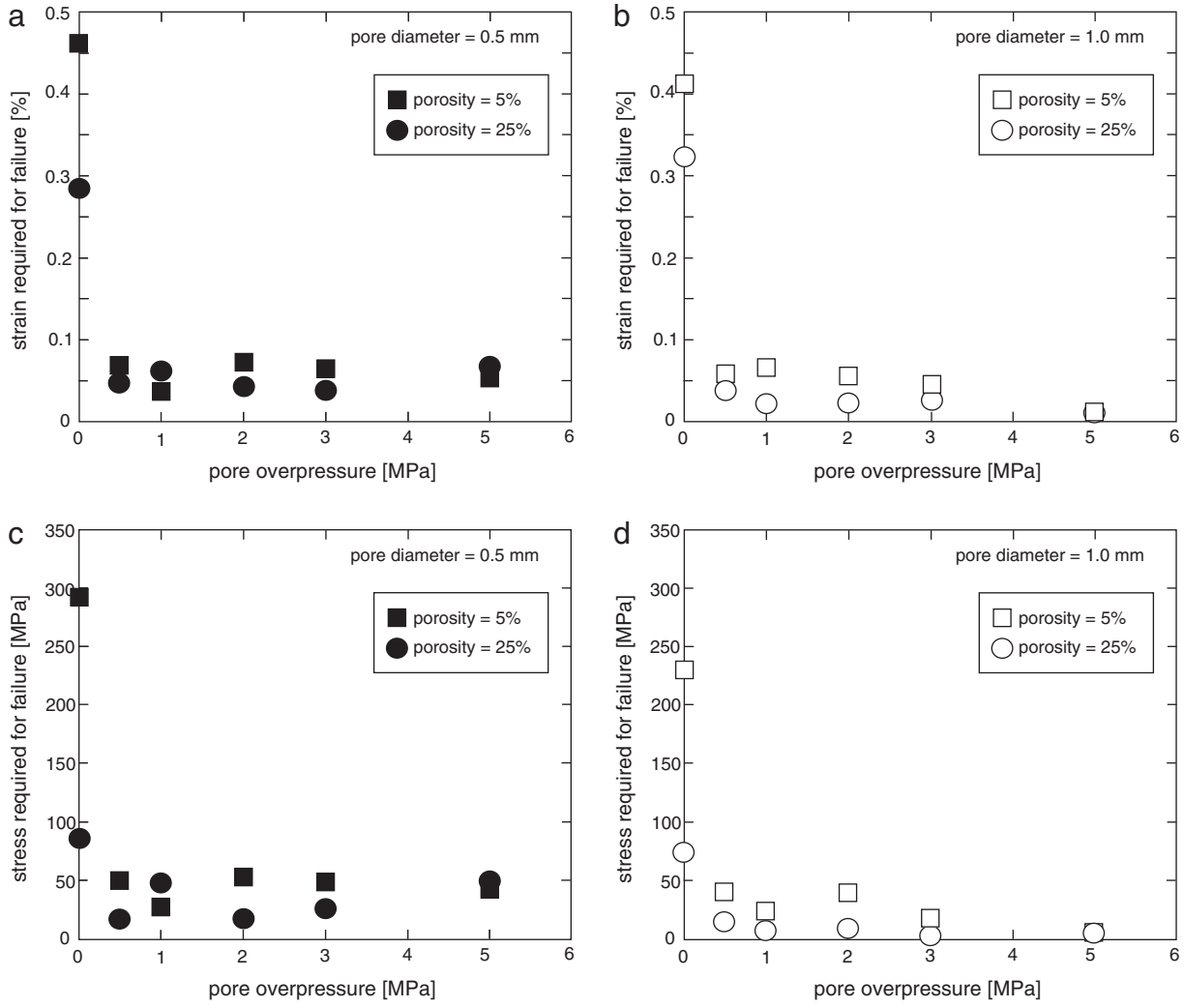

Fig. 7. The results of the Rock Failure and Process Analysis code stochastic modelling: The influence of porosity. Strain (a) and stress (c) required for failure as a function of pore overpressure for a pore diameter of 0.5 mm. Strain (b) and stress (d) required for failure as a function of pore overpressure for a pore diameter of 1.0 mm.

The observed mode of failure in our simulations differs considerably from samples experimentally fragmented as a result of a decompression wave (i.e., in the absence of a differential stress) in which the cylindrical samples are broken perpendicular to their long axis into layers or discs (Fowler et al., 2010); the volume of ash-sized particles during fragmentation depends on the pore overpressure (e.g., Kueppers et al., 2006). Although, we highlight that the requirement for macroscopic failure in our simulations—the tensile failure of stressed elements between neighbouring pores—is similar to the model of Koyaguchi et al. (2008) which stipulates that fragmentation occurs when the tensile stress at a mid-point between two bubbles exceeds a critical value that is inversely proportional to the square root of bubble wall thickness. The difference in mode of failure (decompression wave fragmentation versus magma fracture due to an external differential stress) is likely to produce considerably different volumes of fine particles. Strain localisation during magma fracture (Fig. 6) produces little in the way of fine particles, and only partial fragmentation, while the distributed fragmentation above the fragmentation threshold can produce considerable volumes of fine particles (e.g., Kueppers et al., 2006).

The resultant fracture may influence the progression of volcanic activity in three ways, depicted in the cartoons of Fig. 9b. The cartoons of Fig. 9 show a cross section of a volcano with a central conduit composed of magma containing pressurised pores. While we appreciate that our scenarios are simplifications of the complexity of the porosity distribution in the conduit (e.g., Kennedy et al., 2005; Burgisser et al., 2010; Laumonier et al., 2011; Michaut et al., 2013) we use these examples simply to illustrate the potential implications of our results. The generation of a pore overpressure in the pores of the magma is achieved by partial dome collapse in the cartoons, although the resultant decompression wave is insufficient to fragment the underlying magma. The first set of cartoons (Fig. 9a) depicts a scenario in which there are no external stresses, or the external stresses are dissipated viscously. In this scenario, the conditions for magma fragmentation or magma fracture were not satisfied and there are no secondary consequences of the decompression event. The second set of cartoons (Fig. 9b) depicts a scenario in which external stresses can elastically deform the magma and, although the conditions for fragmentation are not satisfied, the magma fractures due to its low brittle strength in the presence of overpressurised pores. In this scenario, the fracture of the magma is envisaged to have one of three (not necessarily mutually exclusive) consequences. First, if magma failure results in a fracture that cannot access magmas with higher pore pressures, it may assist outgassing (Fig. 9b), at least until it is sealed by any subsequent viscous sintering. We highlight that the ease at which exsolving magma can outgas can reduce the explosivity of subsequent eruptions during a particular period of unrest (e.g., Eichelberger et al., 1986; Woods and Koyaguchi, 1994; Mueller et al., 2008; Castro et al., 2014; Nguyen et al., 2014; Okumura and Sasaki, 2014; Farquharson et al., 2015). We further note that

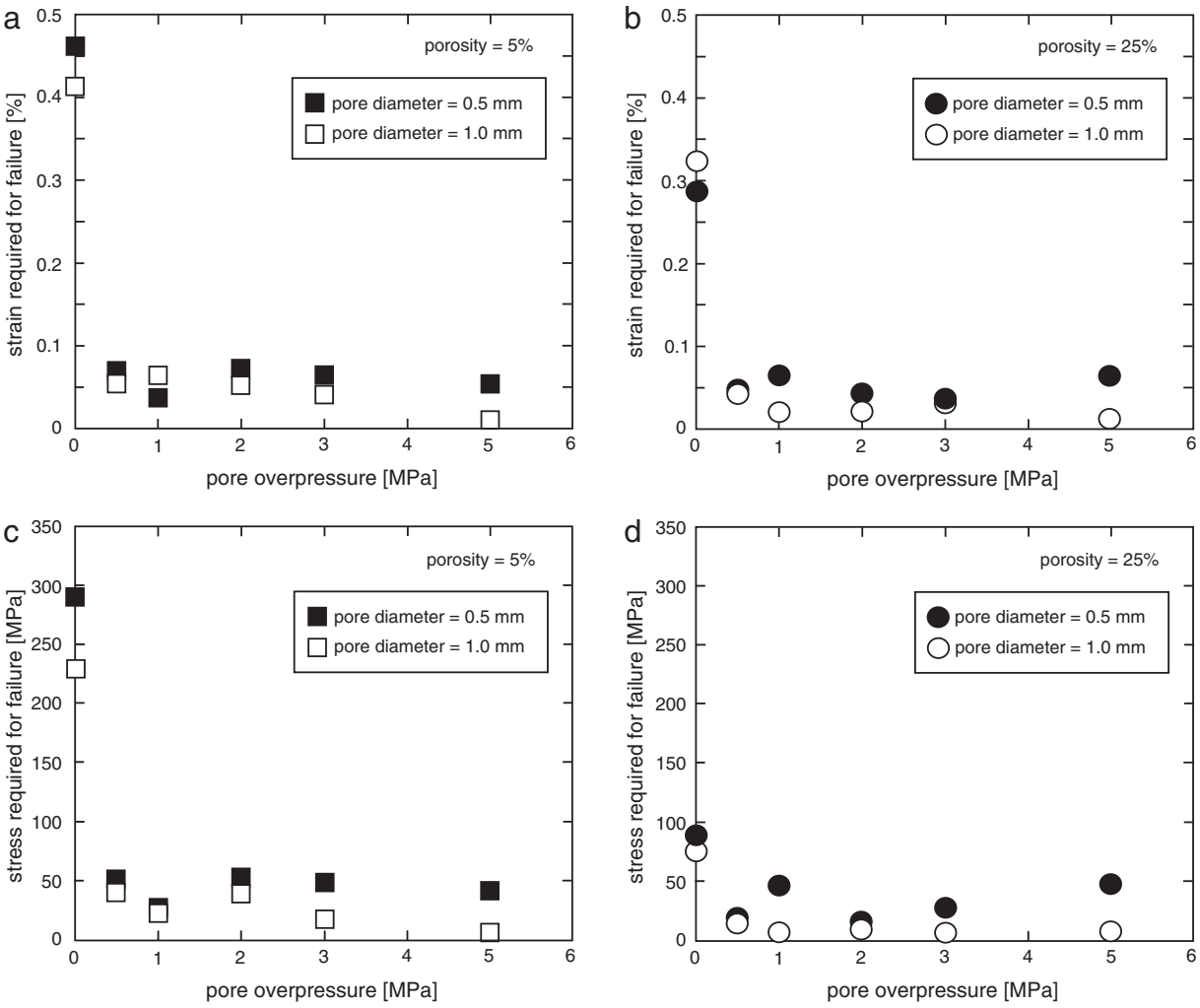

Fig. 8. The results of the Rock Failure and Process Analysis code stochastic modelling: The influence of pore size. Strain (a) and stress (c) required for failure as a function of pore overpressure for a porosity of 5%. Strain (b) and stress (d) required for failure as a function of pore overpressure for a porosity of 25%.

volatiles exsolved from ascending magma may generate a pore overpressure in the country rock (e.g. Heiken et al., 1988). Our model output suggests that, in the presence of a differential stress, these rocks may fracture before the overpressure exceeds their tensile strength. In other words, if there are no other detrimental consequences, fracturing may assist outgassing and reduce the potential for future explosions/eruptions. Second, explosive activity can ensue if the fracture can access magma that, once depressurised, contains pores with pore overpressures above the fragmentation threshold (Fig. 9b). Third, the fracture could structurally destabilise the dome or flank leading to further collapse and the generation of a second decompression wave (Fig. 9b). In the worst-case scenario, outcomes two and three could eventually lead to a larger sustained explosive eruption. Therefore, during periods in which stresses can be accommodated elastically, the fracture of magma, greatly assisted by small pore overpressures, is likely to influence the progression of volcanic activity, promoting explosivity by accessing magma with high pore pressures or diffusing explosivity through outgassing.

We speculate that an external differential stress could also assist rapid decompression fragmentation (i.e., the fragmentation threshold could be lowered in the presence of an external stress). By reducing the fragmentation threshold, less energy is required to fragment the magma, thus allocating more energy to fine particle generation (Kueppers et al., 2006) and ballistic dispersion (Alatorre-Ibargüengoitia et al., 2010). Any additional energy imparted to ballistic dispersion will impact pre-eruptive overpressures predicted at active volcanoes using caprock models. For example, the energy consumed by fragmentation is subtracted in the caprock ejection model of Alatorre-Ibargüengoitia et al. (2010). If we consider that external differential stresses can lower the fragmentation threshold, and thereby reduce the energy required for fragmentation, the predicted overpressures may be lower than the estimations provided by such models.

5. Concluding remarks and perspectives

Hydrostatically, magmas can only fragment above the fragmentation threshold (e.g., Alidibirov and Dingwell, 1996). For example, a fracture may not reach magma with pores containing a high enough pore pressure, or dome collapse may not produce a decompression wave sufficient to fragment the underlying magma. However, if the magma can accommodate external stresses (ubiquitous in volcanic system on the verge of an explosive eruption) in an elastic manner, the presence of a small overpressure (as low as 0.5 MPa) may severely impact the way in which the magma deforms. The fate of the magma in this scenario has been largely overlooked, primarily a result of the limitations of the experimental apparatus currently available. For example, experimental studies of overpressure-driven fragmentation have been performed in the absence of an imposed differential stress, and deformation experiments require that the confining pressure is greater than the pore pressure. Unaffected by these limitations, our modelling has highlighted that the brittle strength, and the strain required for failure, of magma can be reduced by almost an order of magnitude when the pores within the magma contain a pore overpressure as low as 0.5 MPa. The failure

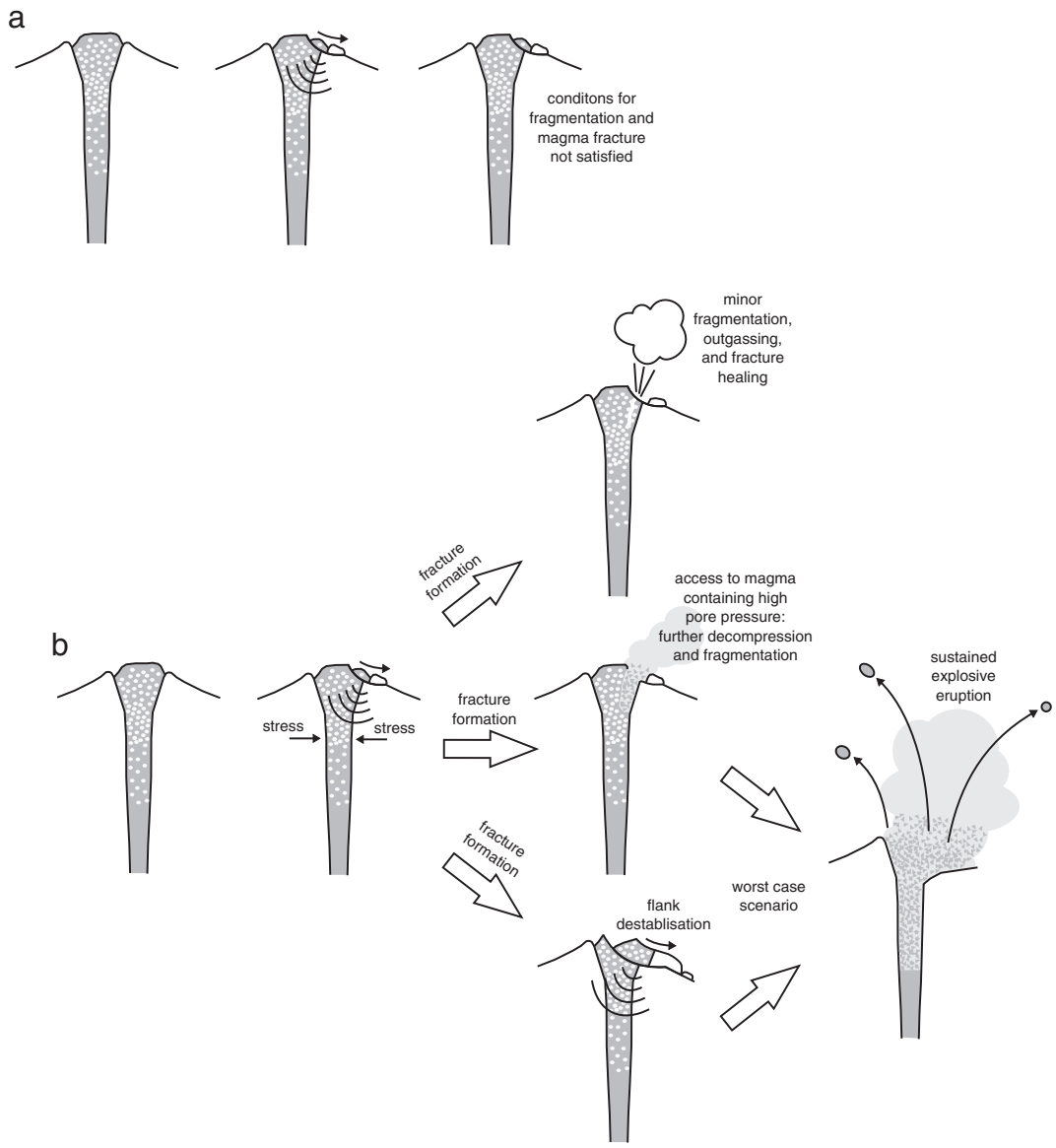

Fig. 9. Cartoons depicting the decompression of the magma within a central conduit composed of magma containing pressurised pores as a result of a partial dome/flank collapse. (a) Set of cartoons depicting a scenario in which there are no external stresses or the external stresses are dissipated viscously. In this case, the conditions for fragmentation or magma fracture are not satisfied. (b) Set of cartoons depicting the same scenario as in panel (a) although, this time, external stresses can be accommodated elastically by the magma. In this case, the conditions for fragmentation are not satisfied, but the conditions for magma fracture are satisfied. The end result is envisaged to be: (1) Minor fragmentation, outgassing, and fracture healing, (2) further decompression and fragmentation, or (3) dome/flank destabilisation. Scenarios (2) and (3) could lead, in the worst-case scenario, to a sustained explosive eruption.

mode of the numerical samples—a throughgoing fracture—differs significantly from layer-by-layer or complete fragmentation above the fragmentation threshold. The resultant fracture could assist outgassing and thus help reduce the explosivity of subsequent eruptions during a particular period of unrest. Alternatively, the fracture may access magmas that then contain pores with pore overpressures above the fragmentation threshold, or promote further dome/flank collapse that can generate a decompression wave capable of magmatic fragmentation, resulting in explosive activity. External stresses, previously unconsidered but invariably present in a dynamic volcanic system, or the stress perturbations likely to accompany any unrest activity, may therefore play a large role in the development and cessation of explosive activity.

Acknowledgements

Michael Heap, Tao Xu, and Chong-feng Chen acknowledge the support of a Partenariats Hubert Curien (PHC) Xu Guangqi grant (grant number 32195NC), managed by Campus France and supported by the Ministry of Foreign Affairs (MAE) in France and the French Institute of the Chinese Embassy of France in China. Michael Heap and Ben Kennedy acknowledge a Hubert Curien Partnership (PHC) Dumont d'Urville grant (grant number 31950RK), funded and implemented by the New Zealand Ministry of Business, Innovation and Employment (MBIE), the Royal Society of New Zealand, and the Ministry of Foreign Affairs (MAEDI) and the Ministry of Higher Education and Research (MENESR) in France. Tao Xu acknowledges the National Natural Science Foundation of China (grant number 51474051). the National Basic Research Programme of China (grant number 2013CB227900) and Fundamental Research Funds for the Central Universities of China (grant number N130501002). Alexandra Kushnir acknowledges a Postgraduate Scholarship-Doctoral (CGS D3) provided by the Natural Sciences and Engineering Research Council of Canada (NSERC) (number CGSD3-444207-2013). Funding for Ben Kennedy was additionally provided by Marsden Fast Start (09-UO-017C) grant. This paper has benefitted from discussions with Yan Lavallée and Jamie Farquharson. This paper has greatly benefitted from constructive reviews by Helge Gonnermann, Ulrich

Kueppers, Takehiro Koyaguchi, one anonymous reviewer, and the editor, Joan Martí.

References

Alatorre-Ibargüengoitia, M.A., Scheu, B., Dingwell, D.B., Delgado-Granados, H., Taddeucci, J., 2010. Energy consumption by magmatic fragmentation and pyroclast ejection during Vulcanian eruptions. Earth Planet. Sci. Lett. 291, 60–69.

Alidibirov, M., Dingwell, D.B., 1996. High temperature fragmentation of magma by rapid decompression. Nature 380, 146–149.

Baud, P., Zhu, W., Wong, T.-F., 2000. Failure mode and weakening effect of water on sandstone. J. Geophys. Res. 105, 16371–16389.

Brace, W.F., Paulding, B.W., Scholz, C.H., 1966. Dilatancy in the fracture of crystalline rocks. J. Geophys. Res. 71, 3939–3953.

Brantut, N., Heap, M.J., Meredith, P.G., Baud, P., 2013. Time-dependent cracking and brittle creep in crustal rocks: a review. J. Struct. Geol. 52, 17–43.

Burgisser, A., Poussineau, S., Arbaret, L., Druitt, T.H., Giachetti, T., Bourdier, J.-L., 2010. Pre-explosive conduit conditions of the 1997 Vulcanian explosions at Soufrière Hills Volcano, Montserrat: I. Pressure and vesicularity distributions. J. Volcanol. Geotherm. Res. 194, 27–41.

Castro, J., Bindeman, I.N., Tuffen, H., Schipper, C.I., 2014. Explosive origin of silicic lava: textural and δD–H_2O evidence for pyroclastic degassing during rhyolite effusion. Earth Planet. Sci. Lett. 405, 52–61.

Cole, P.D.S., P., H., Odbert, M., Stinton, A.J., 2014. Vulcanian explosions at Soufriere Hills Volcano, Montserrat between 2008 and 2010. In: Wadge, G., Robertson, R.E.A., Voight, B. (Eds.), The Eruption of Soufrière Hills Volcano, Montserrat From 2000 to 2010. Geological Society Memoirs, London, pp. 93–111.

Cordonnier, B., Caricchi, L., Pistone, M., Castro, J., Hess, K.-U., Gottschaller, S., Manga, M., Dingwell, D.B., Burlini, L., 2012. The viscous-brittle transition of crystal-bearing silicic melt: direct observation of magma rupture and healing. Geology 40, 611–614.

Dingwell, D.B., 1996. Volcanic dilemma—flow or blow? Science 273, 1054–1055.

Dingwell, D.B., Webb, S.L., 1990. Relaxation in silicate melts. Eur. J. Mineral. 2, 427–449.

Druitt, T.H., et al., 2002. Episodes of cyclic Vulcanian explosive activity with fountain collapse at Soufriere Hills Volcano, Montserrat. In: Druitt, T.H., Kokelaar, B.P. (Eds.), The Eruption of Soufriere Hills Volcano, Montserrat, From 1995 to 1999. Geological Society, London, Memoirs, London, pp. 281–306.

Eichelberger, J.C., Carrigan, C.R., Westrich, H.R., Price, P.H., 1986. Non-explosive silicic volcanism. Nature 323, 598–602.

Farquharson, I.J., Heap, M.J., Varley, N., Baud, P., Reuschlé, T., 2015. Permeability and porosity relationships of edifice-forming andesites: a combined field and laboratory study. J. Volcanol. Geotherm. Res. 297, 52–68.

Fowler, A.C., Scheu, B., Lee, W.T., McGuinness, M.J., 2010. A theoretical model of the explosive fragmentation of vesicular magma. Proc. R. Soc. Lond. A 466 (731), 752.

Gerst, A., Savage, M.K., 2004. Seismic anisotropy beneath Ruapehu Volcano: a possible eruption forecasting tool. Science 306, 1543–1547.

Gonnermann, H.M., Manga, M., 2003. Explosive volcanism may not be an inevitable consequence of magma fragmentation. Nature 426, 432–435.

Gonnermann, H.M., Manga, M., 2012. Dynamics of magma ascent in the volcanic conduit. In: Fagents, S.A., G. T. K. P., Lopes, R.M.C. (Eds.), Modeling Volcanic Processes: The Physics and Mathematics of Volcanism. Cambridge University Press, Cambridge.

Heap, M.J., Baud, P., Meredith, P.G., Vinciguerra, S., Bell, A.F., Main, I.G., 2011. Brittle creep in basalt and its application to time-dependent volcano deformation. Earth Planet. Sci. Lett. 307, 71–82.

Heap, M.J., Xu, T., Chen, C.-f., 2014. The influence of porosity and vesicle size on the brittle strength of volcanic rocks and magmas. Bull. Volcanol. 76, 856. http://dx.doi.org/10.1007/s00445-014-0856-0.

Heiken, G., Wohletz, K., Eichelberger, J.C., 1988. Fracture fillings and intrusive pyroclasts, Inyo Domes, California. J. Geophys. Res. 93, 4335–4350.

Hoek, E., Bieniawski, Z.T., 1965. Brittle fracture propagation in rock under compression. Int. J. Fract. 1, 137–155.

Jaeger, J., Cook, N.G.W., Zimmerman, R., 2007. Fundamentals in Rock Mechanics (4th Edition). 4th ed. Blackwell Publishing, London.

Jaupart, C., 1998. Gas loss from magmas through conduit walls during eruption. Geol. Soc. Lond., Spec. Publ. 145, 73–90.

Kendrick, J.E., Lavallée, Y., Hess, K.-U., Heap, M.J., Gaunt, H.E., Meredith, P.G., Dingwell, D.B., 2013. Tracking the permeable porous network during strain-dependent magmatic flow. J. Volcanol. Geotherm. Res. 260, 117–126.

Kendrick, J.E., Lavallée, Y., Hirose, T., Di Toro, G., Hornby, A.J., De Angelis, S., Dingwell, D.B., 2014. Volcanic drumbeat seismicity caused by stick-slip motion and magmatic frictional melting. Nat. Geosci. http://dx.doi.org/10.1038/ngeo2146.

Kennedy, B.M., Jellinek, A.M., Russell, J.K., Nichols, A.R.L., Vigouroux, N., 2010. Time- and temperature-dependent conduit wall porosity: a key control on degassing and explosivity at Tarawera volcano, New Zealand. Earth Planet. Sci. Lett. 299, 126–137.

Kennedy, B.M., Spieler, O., Scheu, B., Kueppers, U., Taddeucci, J., Dingwell, D.B., 2005. Conduit implosion during Vulcanian eruptions. Geology 33, 581–584.

Koyaguchi, T., Scheu, B., Mitani, N.K., Melnik, O., 2008. A fragmentation criterion for highly viscous bubbly magmas estimated from shock tube experiments. J. Volcanol. Geotherm. Res. 178, 58–71.

Kueppers, U., Scheu, B., Spieler, O., Dingwell, D.B., 2006. Fragmentation efficiency of explosive volcanic eruptions: a study of experimentally generated pyroclasts. J. Volcanol. Geotherm. Res. 153, 125–135.

Lacroix, P., Amitrano, D., 2013. Long-term dynamics of rockslides and damage propagation inferred from mechanical modeling. J. Geophys. Res. 118, 2292–2307.

Laumonier, M., Arbaret, L., Burgisser, A., Champallier, R., 2011. Porosity redistribution enhanced by strain localisation in crystal-rich magmas. Geology 39, 715–718.

Lavallée, Y., Meredith, P.G., Dingwell, D.B., Hess, K.-U., Wassermann, J., Cordonnier, B., Gerik, A., Kruhl, J.H., 2008. Seismogenic lavas and explosive eruption forecasting. Nature 453. http://dx.doi.org/10.1038/nature06980.

Lavallée, Y., Benson, P.M., Heap, M.J., Hess, K.-U., Flaws, A., Schillinger, B., Meredith, P.G., Dingwell, D.B., 2013. Reconstructing magma failure and the degassing network of dome-building eruptions. Geology 41, 515–518.

Lemaitre, J., Chaboche, J.-L., 1990. Mechanics of Solid Materials. Cambridge University Press, Cambridge.

Mangan, M.T., Cashman, K.V., Newman, S., 1993. Vesiculation of basaltic magma during eruption. Geology 21, 157–160.

Martel, C., Dingwell, D.B., Spieler, O., Pichavant, M., Wilke, M., 2000. Fragmentation of foamed silicic melts: an experimental study. Earth Planet. Sci. Lett. 178, 47–58.

Martel, C., Dingwell, D.B., Spieler, O., Pichavant, M., Wilke, M., 2001. Experimental fragmentation of crystal- and vesicle-bearing silicic melts. Bull. Volcanol. 63, 398–405.

Martí, J., Soriano, C., Dingwell, D.B., 1999. Tube pumices as strain markers of the ductile–brittle transition during magma fragmentation. Nature 402, 650–653.

Massol, H., Jaupart, C., 1999. The generation of gas overpressure in volcanic eruptions. Earth Planet. Sci. Lett. 166, 57–70.

Melnik, O., Barmin, A.A., Sparks, R.S.J., 2005. Dynamics of magma flow inside volcanic conduits with bubble overpressure buildup and gas loss through permeable magma. J. Volcanol. Geotherm. Res. 143, 53–68.

Michaut, C., Bercovici, D., Sparks, R.S.J., 2009. Ascent and compaction of gas rich magma and the effects of hysteretic permeability. Earth Planet. Sci. Lett. 282, 258–267.

Michaut, C., Ricard, Y., Bercovici, D., Sparks, R.S.J., 2013. Eruption cyclicity at silicic volcanoes potentially caused by magmatic gas waves. Nat. Geosci. 6, 856–860.

Mueller, S., Scheu, B., Spieler, O., Dingwell, D.B., 2008. Permeability control on magma fragmentation. Geology 36, 399–402.

Navon, O., Lyakhovsky, V., 1998. Vesiculation processes in silicic magmas. Geol. Soc. Lond., Spec. Publ. 145, 27–50.

Nguyen, C.T., Gonnermann, H.M., Houghton, B.F., 2014. Explosive to effusive transition during the largest volcanic eruption of the 20th century (Novarupta 1912, Alaska). Geology. http://dx.doi.org/10.1130/G35593.35591.

Okumura, S., Sasaki, O., 2014. Permeability reduction of fractured rhyolite in volcanic conduits and its control on eruption cyclicity. Geology 42, 843–846.

Papale, P., 1999. Strain-induced magma fragmentation in explosive eruptions. Nature 397, 425–428.

Proussevitch, A., Sahagian, D., 2005. Bubbledrive-1: a numerical model of volcanic eruption mechanisms driven by disequilibrium magma degassing. J. Volcanol. Geotherm. Res. 143, 89–111.

Roman, D.C., Moran, S.C., Power, J.A., Cashman, K.V., 2004. Temporal and spatial variation of local stress fields before and after the 1992 eruptions of Crater Peak Vent, Mount Spurr Volcano, Alaska. Bull. Seismol. Soc. Am. 94, 2366–2379.

Sammis, C.G., Ashby, M.F., 1986. The failure of brittle porous solids under compressive stress states. Acta Metall. 34, 511–526. http://dx.doi.org/10.1016/0001-6160(1086)90087-90088.

Scheu, B., Kueppers, U., Mueller, S., Spieler, O., Dingwell, D.B., 2008. Experimental volcanology on eruptive products of Unzen volcano. J. Volcanol. Geotherm. Res. 175, 110–119.

Scholz, C.H., 1968. Microfracturing and the inelastic deformation of rock in compression. J. Geophys. Res. 73, 1417–1432.

Shields, J.K., Mader, H.M., Pistone, M., Caricchi, L., Floess, D., Putlitz, B., 2014. Strain-induced outgassing of three-phase magmas during simple shear. J. Geophys. Res. http://dx.doi.org/10.1002/2014JB011111.

Sparks, R.S.J., 1978. The dynamics of bubble formation and growth in magmas: a review and analysis. J. Volcanol. Geotherm. Res. 3, 1–37.

Sparks, R.S.J., 1996. Causes and consequences of pressurisation in lava dome eruptions. Earth Planet. Sci. Lett. 150, 177–189.

Spieler, O., Kennedy, B., Kueppers, U., Dingwell, D.B., Scheu, B., Taddeucci, J., 2004. The fragmentation threshold of pyroclastic rocks. Earth Planet. Sci. Lett. 226, 139–148.

Stix, J., Torres, R.C., Narváez, L., Cortés, G.P., Raigosa, J.A., Gómez, D., Castonguay, R., 1997. A model of vulcanian eruptions at Galeras volcano, Columbia. J. Volcanol. Geotherm. Res. 77, 285–303.

Tait, S., Jaupart, C., Vergniolle, S., 1989. Pressure, gas content and eruption periodicity of a shallow crystallising magma chamber. Earth Planet. Sci. Lett. 92, 107–123.

Tang, C.A., 1997. Numerical simulation of progressive rock failure and associated seismicity. Int. J. Rock Mech. Min. Sci. 34, 249–261.

Tang, C.A., Tham, L.G., Lee, P.K.K., Yang, T.H., Li, L.C., 2002. Coupled analysis of flow, stress and damage (FSD) in rock failure. Int. J. Rock Mech. Min. Sci. 39, 477–489.

Tang, C.A., Huang, M.L., Zhao, X.D., 2003. Weak zone related seismic cycles in progressive failure leading to collapse in brittle crust. Pure Appl. Geophys. 160, 2319–2328.

Tang, C.A., Xu, T., Yang, T.H., Liang, Z.Z., 2004. Numerical investigation of the mechanical behavior of rock under confining pressure and pore pressure. Int. J. Rock Mech. Min. Sci. 41, 336–341.

Toramaru, A., 1989. Vesiculation process and bubble size distributions in ascending magmas with constant velocities. J. Geophys. Res. 94 (B12), 17523–17542.

Tuffen, H., Dingwell, D.B., Pinkerton, H., 2003. Repeated fracture and healing of silicic magma generate flow banding and earthquakes? Geology 31, 1089–1092.

Vasseur, J., Wadsworth, F.B., Lavallée, Y., Hess, K.-U., Dingwell, D.B., 2013. Volcanic sintering: timescales of viscous densification and strength recovery. Geophys. Res. Lett. 40, 5658–5664.

Walker, G.P.L., Croasdale, R., 1970. Two Plinian-type eruptions in the Azores. J. geol. Soc. 127, 17–55.

Wang, S.Y., Sloan, S.W., Fityus, S.G., Griffiths, D.V., Tang, C.A., 2013. Numerical modeling of pore pressure influence on fracture evolution in brittle heterogeneous rocks. Rock Mech. Rock. Eng. 46, 1165–1182.

Weibull, W., 1951. A statistical distribution function of wide applicability. J. Appl. Mech. 18, 293–297.
Wong, T.-f., Wong, R.H.C., Chau, K.T., Tang, C.A., 2006. Microcrack statistics, Weibull distribution and micromechanical modeling of compressive failure in rock. Mech. Mater. 38, 664–681.
Woods, A.W., Koyaguchi, T., 1994. Transitions between explosive and effusive eruptions of silicic magmas. Nature 370, 641–644.
Xu, T., Tang, C.A., Yang, T.H., Zhu, W.C., Liu, J., 2006. Numerical investigation of coal and gas outbursts in underground collieries. Int. J. Rock Mech. Min. Sci. 43, 905–919.
Xu, T., Tang, C.A., 2008. Modeling of stress-induced permeability evolution and damage of rock. Adv. Mater. Res. 33–37, 609–616.
Xu, T., Tang, C.-A., Zhao, J., Li, L., Heap, M.J., 2012. Modelling the time-dependent rheological behaviour of heterogeneous brittle rocks. Geophys. J. Int. 189, 1781–1796.
Yokoo, A., Tameguri, T., Iguchi, M., 2009. Swelling of a lava plug associated with a Vulcanian eruption at Sakurajima Volcano, Japan, as revealed by infrasound record: case study of the eruption on January 2, 2007. Bull. Volcanol. 71, 619–630.
Zhang, Y., 1999. A criterion for the fragmentation of bubbly magma based on brittle failure theory. Nature 402, 648–650.